DOI 10.1515/nanoph-2013-0027 — Nanophotonics 2014; 3(4-5): 329–341

**Review article**

Raji Shankar and Marko Lončar*

# Silicon photonic devices for mid-infrared applications

**Abstract:** The mid-infrared (IR) wavelength region (2–20 μm) is of great interest for a number of applications, including trace gas sensing, thermal imaging, and free-space communications. Recently, there has been significant progress in developing a mid-IR photonics platform in Si, which is highly transparent in the mid-IR, due to the ease of fabrication and CMOS compatibility provided by the Si platform. Here, we discuss our group's recent contributions to the field of silicon-based mid-IR photonics, including photonic crystal cavities in a Si membrane platform and grating-coupled high-quality factor ring resonators in a silicon-on-sapphire (SOS) platform. Since experimental characterization of microphotonic devices is especially challenging at the mid-IR, we also review our mid-IR characterization techniques in some detail. Additionally, pre- and post-processing techniques for improving device performance, such as resist reflow, Piranha clean/HF dip cycling, and annealing are discussed.

**Keywords:** mid-infrared; silicon photonics; ring resonators.

***Corresponding author: Marko Lončar,** School of Engineering and Applied Sciences, Harvard University, Cambridge, MA 02138, USA, e-mail: loncar@seas.harvard.edu
**Raji Shankar:** School of Engineering and Applied Sciences, Harvard University, Cambridge, MA 02138, USA

**Edited by Michal Lipson**

## 1 Introduction

The mid-infrared (IR) wavelength range (2–20 μm) is of great utility for a number of applications, including chemical bond spectroscopy, trace gas sensing, and medical diagnostics. In particular, part of the mid-IR region (8–20 μm) is often referred to as the "fingerprint region", since many molecules have uniquely identifiable absorption spectra within this wavelength range. Additionally, the mid-IR wavelength region is well-suited for thermal imaging and free-space communications, especially within the atmospheric windows of 3–5 μm and 8–11 μm.

Despite this wealth of applications, the on-chip mid-IR photonics platform needed to access them is relatively undeveloped. While the last 10–15 years have seen the development of high-power, room temperature mid-IR light sources and sensitive mid-IR detectors, little work had been done in developing the passive photonics elements such as waveguides, resonators, splitters, modulators, etc. for the mid-IR. Conventionally, mid-IR photonics has been associated with the III-IV materials used for active optoelectronic devices (lasers and detectors), as well as chalcogenide glasses [1] used for passive photonic elements. However, R. Soref et al. proposed in 2006 [2] that group IV materials (silicon and germanium) are also promising mid-IR materials, as they exhibit low loss through much of the mid-IR. In particular, silicon is an attractive material of choice for the mid-IR, as we can take advantage of extremely well developed fabrication techniques and CMOS compatibility, making the realization of on-chip integrated mid-IR devices more realistic.

In Figure 1, we show the imaginary part of the refractive index of Si, κ, plotted as a function of wavelength (data taken from [3]). Below 6.5 μm, κ is smaller than $10^{-6}$, which offers the potential for strong light confinement in Si devices from 2 to 6.5 μm. Finally, due to the lack of two- and three-photon absorption in the mid-IR, the power density of optical signals propagating in Si waveguides or stored in Si optical cavities can be significantly higher than at the near-IR wavelengths used for telecommunications [4–8]. Because of this, the mid-IR wavelengths afford the opportunity to exploit Si's relatively high third-order optical nonlinearity ($n_2 = 3.6\times10^{-18}$ m$^2$/W [9]) for nonlinear frequency generation applications, since these applications require high pump powers. On-chip four-wave mixing, parametric oscillation, and frequency comb generation should be possible at mid-IR wavelengths in the proper Si platform. On-chip frequency combs would be especially useful for mid-IR sensing and spectroscopic applications, as broadband sources are often required for these applications.

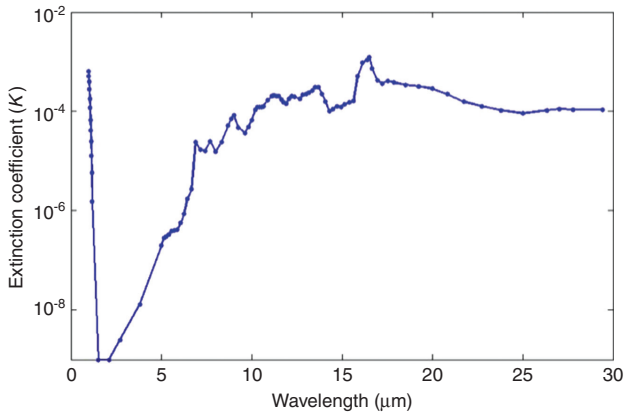


**Figure 1** The extinction coefficient κ as a function of wavelength for silicon. Data taken from [3].

Despite the suitability of Si for mid-IR applications, a different set of experimental challenges are encountered when working at the mid-IR as opposed to at the telecommunications wavelengths, where Si photonics is already well-developed. One relates to fabrication: the silicon-on-insulator (SOI) platform, the standard platform used for on-chip photonics at telecom, is of limited utility at the mid-IR due to the high loss of silicon dioxide (>2 dB/cm) at wavelengths larger than 3.5 μm [3, 4]. One solution is to selectively remove the buried oxide layer under the devices to form suspended structures. This method has been used by our group to make Si photonic crystal cavities operational at 4.5 μm [10, 11], and more recently by researchers at the Universities of St. Andrews and Southampton to make photonic crystal waveguides operational between 2.9 and 3.9 μm [12]. However, for many applications an on-substrate platform is preferred. Because of this, much mid-IR work has been performed in the silicon-on-sapphire (SOS) platform, because of the low losses in sapphire below 5 μm [2, 4]. Researchers at the University of Washington demonstrated the first SOS waveguides operational at 4.5 μm in 2010 [13], and subsequently demonstrated ring resonators operational at 5.5 μm [14]. SOS waveguides operating at 2.75 μm [15] and 5.18 μm [16], ring resonators operating at 2.75 μm [17], and grating couplers operating at 2.75 μm [15, 17] have also been demonstrated. Recently, our group has demonstrated high-quality (Q) factor grating-coupled microring resonators operational at 4.3–4.6 μm, with intrinsic Q-factors of over 200,000 [18]. Other Si-based platforms in which mid-IR waveguides have been demonstrated include Si on porous Si (waveguides operational at 3.39 μm) [19], Si on SiN (waveguides operational at 3.39 μm) [20], SiN on $SiO_2$ (waveguides and couplers operational at 3.7 μm) [21], and Ge on Si (waveguides operational at 5.8 μm) [22]. Finally, researchers at the Massachusetts Institute of Technology have very recently demonstrated an alternate fabrication method to make air-clad pedestal structures out of bulk silicon, and have fabricated waveguides and power splitters operational from 2.5 to 3.7 μm through this process [23].

Building complex optical characterization setups for mid-IR photonic devices is another challenging aspect of working at this wavelength range. Therefore, a discussion of mid-IR photonics is not complete without a discussion of the characterization techniques used to measure the performance of mid-IR photonic devices. Mid-IR beams are invisible, and no true viewing cards (such as those used for the telecom) exist for mid-IR beams (though photo-thermal paper can be used for rough alignment with a high intensity beam). Similarly, mid-IR optical components, such as lenses, polarizers, modulators, etc. are often quite primitive (as well as more expensive) compared to their visible and telecom counterparts. The same goes for mid-IR fibers, which are prone to degradation. Additionally, commercially available quantum cascade lasers (QCLs), the light sources of choice between 4 and 20 μm, are not currently available with fiber coupling options (at shorter wavelengths, there has been much recent promising work on ZBLAN fiber lasers [24]), leading to extra optical elements being necessary to couple light into the fiber. For these reasons, we have focused on free-space coupling methods rather than fiber-coupling methods to introduce light into our cavities. However, many other research groups have demonstrated the use of fiber-coupling to characterize mid-IR silicon devices, mostly through butt-coupling from waveguide into mid-IR fiber, as in [19, 20, 23]. As mid-IR fiber technology evolves, we expect that fiber-coupled devices at the mid-IR will be more common.

In this review, we present our group's recent work on the development of a Si mid-IR photonics platform, mainly in the form of mid-IR microresonators, as well as the development of tools to effectively characterize mid-IR photonic devices. First, we discuss the design, fabrication, and characterization of mid-IR photonics crystal cavities in a Si membrane platform. Then we discuss the phenomenon of optical bistability in these devices, and the role of surface treatments in decreasing absorption loss and mitigating bistability. Next, we describe the design, fabrication, and characterization of mid-IR ring resonators in a silicon-on-sapphire (SOS) platform. This is a particularly suitable platform for integrated mid-IR photonics in the 2–5 μm range. We conclude with an outlook and discussion of integrated mid-IR photonics devices in Si, and consider the feasibility of nonlinear frequency conversion at longer wavelengths.

## 2 Mid-IR Photonic Crystal cavities in Si

High quality factor (Q) and low mode volume optical resonators in the mid-IR are of interest for many applications, including trace gas sensing and optical interconnects. We were particularly interested in photonic crystal cavities, because of their small footprint and the fact that they can be easily characterized through free-space coupling methods. Additionally, we decided to work with the SOI platform, which meant that we needed to make suspended devices using selective undercutting of the oxide layer, which is easily done for planar photonic crystal cavities. Our photonic crystal cavity of choice, the so-called L3 photonic crystal cavity [25], consists of a two-dimensional hexagonal photonic crystal lattice of air holes (periodicity $a$ =1.34 μm, hole radius $r$=353 nm) in a Si slab (thickness $t$ =500 nm), with three central air holes removed to form a line defect [10]. To maximize the Q of the cavity, the air holes on either side of the line defect were shifted outward by a shift $s$=0.2$a$, or approximately 270 nm. The optimized cavity design supports a resonance at a wavelength $\lambda$=4.615 μm, with a Q factor of 66,000.

The devices were fabricated on a silicon-on-insulator (SOI) substrate (SOITEC Inc.), with a device layer thickness of 500 nm and $SiO_2$ layer thickness of 3 μm. A standard 100 kV electron beam lithography tool (Elionix ELS-7000) was used to define patterns in ZEP (Zeon Corp.), a positive electron beam resist. Etching was performed in a reactive ion etcher (STS-ICP-RIE) using $C_4F_8$, $SF_6$, and $H_2$ gases. The devices were undercut using a 7:1 buffered oxide etch for 45 min. A scanning electron micrograph of a completed device is shown in Figure 2.

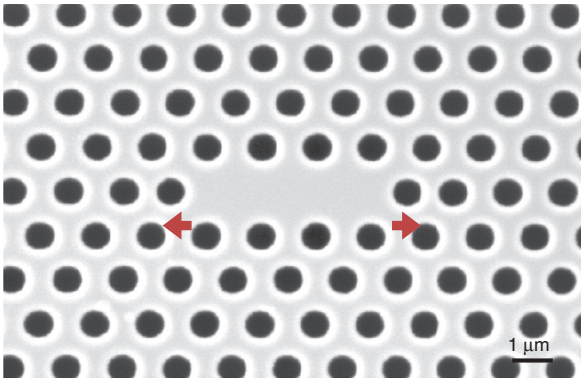


**Figure 2** A scanning electron microscope (SEM) image of a mid-infrared L3 photonic crystal cavity fabricated in silicon , with hole periodicity $a$=1.34 μm, hole radius $r$=350 nm, thickness $t$=500 nm, and hole shift $s$=0.15$a$. Red arrows indicate air hole shift.

We used the resonant scattering method [26, 27] to test our cavities (Figure 3). Light from a tunable quantum cascade laser (QCL) with emission from 4.315 to 4.615 μm (Daylight Solutions, Inc.) is sent into a ZnSe objective lens with numerical aperture (NA) of 0.22 and focused onto the sample, which is placed so that the cavity mode polarization is oriented at 45° with respect to the E-field of the laser spot [10]. Since the QCL emission is invisible, a yellow HeNe laser beam was aligned to the path of the QCL and then used to align the rest of the optics. The sample is mounted on an automatic micropositioner stage, which can be scanned using computer control. The light that is coupled and re-emitted by the photonic crystal cavities is backscattered into the ZnSe objective, and then travels through a second polarizer (the analyzer) which is cross-polarized with respect to the input polarizer, before being focused onto a thermoelectrically cooled mercury cadmium telluride (MCT) detector. This cross-polarization method enhances the signal-to-background ratio of the resonantly scattered light (the signal) to the non-resonantly scattered light (the background). Depending on this ratio, the resonance peak can appear as a Lorentzian or a Fano lineshape caused by the phase shift between the resonant (re-emitted by cavity) and non-resonant components of the back-scattered signal [28].

The experimental results for the photonic crystal cavities are shown in Figure 4A [10]. Photonic crystal cavity modes are found within the range of 4.38–4.42 μm. As predicted by theory, the cavity resonance wavelengths redshift as the air hole shift $s$ is increased from zero to a maximum of $s$=0.225$a$. A peak Q-factor of 13,600 is found

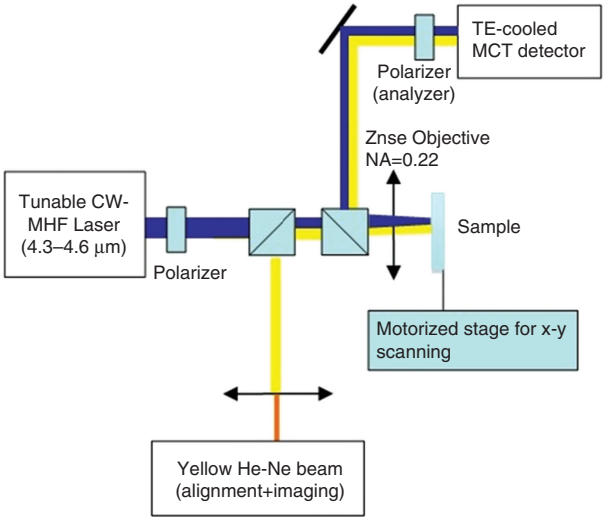


**Figure 3** A schematic of the resonant scattering setup used to measure photonic crystal cavity spectra. The blue line indicates the QCL beam path; the yellow line indicates the HeNe beam path. Adapted from reference [10].

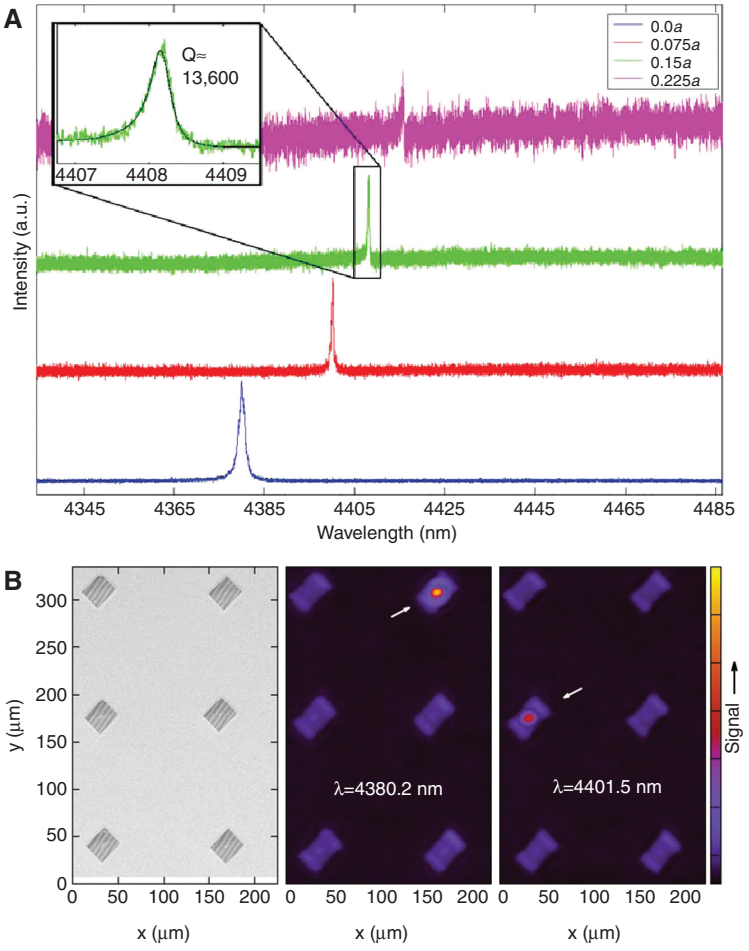


**Figure 4** (A) Resonant scattering spectra (taken at low input power) of photonic crystal cavities with air hole shifts $s=0$, $s=0.075a$, $s=0.15a$, $s=0.225a$, where $a$ is the periodicity. Inset shows Fano fit to $s=0.15a$ cavity. (B) Mid-infrared scanning resonant scattering image of an array of cavities. Scanning electron micrograph is provided for comparison. When our laser is tuned to one of the cavity resonances, and scanned over the cavity array, only the cavity in resonance with the laser lights up. For example, when 4380.2 nm light, corresponding to the resonance of the top right cavity in the center panel, is scanned over the array, only that cavity appears "ON", featuring a bright spot in its center. Alternatively, when the laser is tuned to 4401.5 nm and scanned over the array, only the middle-left cavity (rightmost panel) resonates. Adapted from reference [10].

for $s=0.15a$. The inset in Figure 4A shows the measured Fano lineshape of the resonance. These spectra were taken at low input power to avoid the effects of optical bistability (discussed in the next section). In order to image the spatial profile of optical cavities, we developed the mid-IR scanning resonant scattering microscopy technique [10, 29]. Laser light (at an arbitrary wavelength) was focused on the sample, which was scanned in the x- and y-directions using computer-controlled micropositioners. Reflected light was collected using the same lens and detected using the MCT detector. This procedure allows us to easily identify the cavities since they scatter more light than the background (Figure 4B). Once outlines of the cavities are identified, the laser is focused on the center of one of the cavities and its wavelength is swept to obtain a resonant scattering spectrum (Figure 4A). Finally, the image of the optical mode can be obtained by tuning the laser to the cavity resonance and scanning the sample holder stages while recording the resonantly scattered signal at each position. Images obtained using this approach are shown in Figure 4B. It can be seen that the cavity regions light up at the wavelengths corresponding to the resonance peak in the wavelength scan. This imaging approach can be seen as a single-pixel mid-infrared camera, allowing for the visualization of fabricated structures and resonant modes without the use of expensive mid-IR cameras.

In Figure 5 [10], we show a spectrum and scanning mid-IR images of additional resonances that were observed in another sample. These photonic crystal cavities on this sample were placed relatively close together, with a separation of 22 μm in the y-direction. Resonant scattering spectra of these cavity devices show two extra

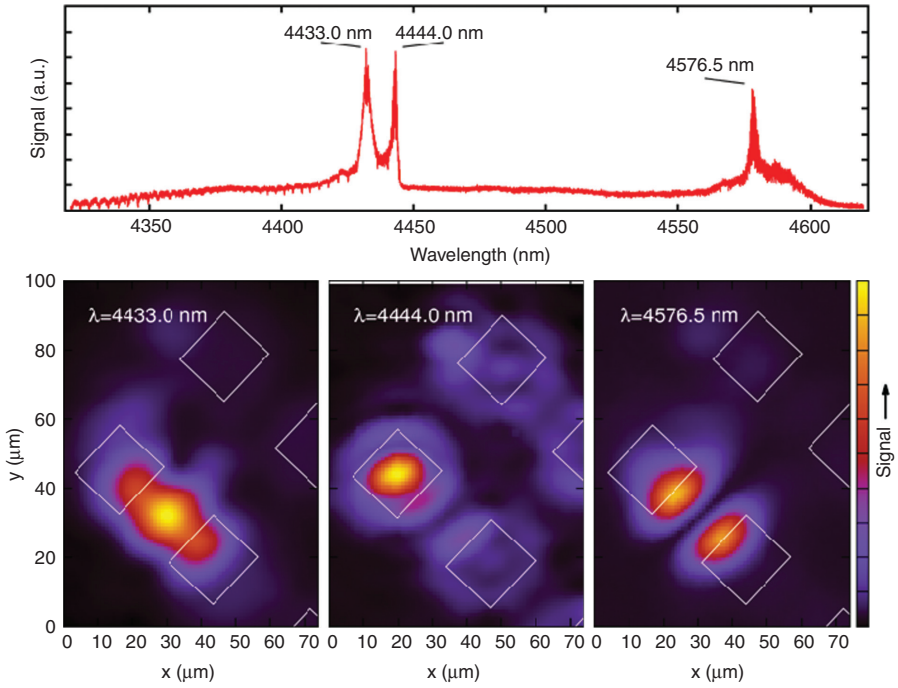


**Figure 5** Resonant scattering spectrum showing peaks corresponding to two inter-cavity Fabry-Perot resonances (4430.0 nm and 4567.5 nm) and one L3 photonic crystal cavity resonance (4444.0 nm). (B) Scanning images of Fabry-Perot resonances (leftmost and rightmost panels) and photonic crystal cavity resonance (center panel). Taken from reference [10].

peaks (at 4.433 μm and 4.567 μm) in addition to the cavity resonance peak (4.444 μm). Using scanning resonant scattering microscopy, we were able to image these modes and attribute them to the inter-cavity resonances of the Fabry-Perot cavity formed between two adjacent photonic crystal structures (Figure 5B): one resonance has an antinode (leftmost panel, 4.433 μm) and the other one has a node (rightmost panel, 4.567 μm) in the center of the inter-cavity region. The resonance at 4.444 μm (center panel in Figure 5B) corresponds to a bonafide resonance of the L3 photonic crystal cavity.

Using mid-IR scanning resonant scattering microscopy, we can visualize the spatial profile of resonances observed in the collected spectrum and unambiguously attribute them to the modes of different cavities. This approach results in a very powerful tool that overcomes many of the inherent experimental difficulties of the mid-IR.

## 3 Bistability in mid-IR photonic crystal cavities

At higher input powers than those shown in Figure 3, we saw the evidence of optical bistability in our cavities [11]. Optical bistability is a well-known phenomenon in Si microresonators at telecom wavelengths [30–34]. Since the refractive index of Si can change either directly or indirectly due to incident light intensity, the resonance wavelength of a microresonator also changes with a buildup of optical power in the resonator. This results in a positive feedback process that allows the resonator to act as a bistable switch, with an off-resonance, or "empty" state and an on-resonance, or "loaded" state. The power dependence of the refractive index can be attributed to various effects, including the $\chi 3$ of Si, free-carrier dispersion, and the thermo-optic effect. Strong light confinement in nano-photonic devices at telecom wavelengths (e.g., 1.55 μm), and in high quality (Q) factor photonic crystal cavities in particular, results in two-photon absorption processes which lead to a pronounced thermo-optic effect due to free-carrier absorption. This limits the operation of Si-based photonic devices to low powers at the telecom wavelength range.

However, multiphoton absorption is unlikely at our wavelength range, as at least 4 photons are needed to overcome the Si bandgap energy. Furthermore, in our case the bistability is due to a redshift of cavity resonance with increasing power, which narrows down the possible origins of the nonlinearity to thermal effects and $\chi 3$ effects [35, 36]. Thermal effects occur when light is absorbed into the cavity, changing the temperature of the cavity and hence the refractive index through the

thermo-optic effect, resulting in a red-shift of the cavity resonance in the case of Si (thermo-optic coefficient of $1.8\times10^{-4}$ $K^{-1}$). Different absorption mechanisms that could lead to the thermo-optic effect in Si at mid-IR wavelengths include the linear absorption of Si (phonon-assisted absorption), free-carrier absorption, various surface absorption effects, and the absorption from native oxide formed on Si surfaces. Free carrier absorption is unlikely in our highly resistive Si wafer (ρ=50 Ω·cm) with a linear loss constant of $\alpha<0.002$ $cm^{-1}$ at 4.5 μm [37]. Similarly, the intrinsic Si absorption is negligible at our wavelength range with an absorption coefficient of 0.04 $cm^{-1}$ at 4.5 μm [3]. This leaves surface effects and absorption due to the thin native oxide layer as the possible origin of the observed bistability. In addition, direct nonlinear processes due to the $\chi3$ of Si (the Kerr effect in particular) could explain our results. However, the Kerr effect results in an instantaneous change of refractive index, whereas thermally-induced refractive index changes occur on a much slower time scale (on the order of μs). We performed time domain measurements in order to separate these effects and established that our nonlinearity was primarily thermal [35, 36, 38]. By modulating the input laser signal with a sine wave and looking for distortion in the output signal [35, 38] due to bistablity, we were able to establish that 200 kHz was the modulation frequency at which all bistability-induced distortion disappeared, indicating that instantaneous $\chi3$ effects could not be the cause of our bistability [11]. The corresponding thermal time constant, 5 μs, is also consistent with finite-element modeling of thermal effects in our cavities.

In order to identify the impact of different surface effects on the bistability, we performed various microelectronic treatments to alter the surface properties of our cavities [11]. An HF dip [11] was performed in order to remove native oxide. This resulted in an increase of Q-factor from about 11,500 to 21,000, but bistability was still present in the cavity at high input powers. Next, we performed a Piranha clean/HF dip cycle [11, 39, 40] as proposed by Borselli et al. in [39] in order to reduce surface state absorption and surface roughness. This had a minimal effect on Q, and the bistability was still present after this treatment. An anneal at 500°C (for two hours) in air [11, 41] was also performed, resulting in an increase in Q from 21,000 to 29,300, indicating that water moisture likely has a considerable absorptive effect at 4-5 μm. After this first annealing step, the bistability was still present at high input powers. Finally, the cavities were annealed in an $N_2$ environment in order to desorb hydrogen from the surface of the Si [41]. After annealing our devices with $N_2$ flowing through our furnace at 500°C for 2 h, we noticed that the cavity spectrum no longer had the characteristic bistable lineshape (blue curve, taken before annealing) and instead was more Fano-like (red curve) at similar input powers (Figure 6). The Q-factor did not change measurably after annealing, reaching a value of 25,600.

To confirm that the cavity was no longer bistable after the $N_2$ anneal, we compared input power vs. output power hysteresis loops taken before and after the anneal (inset, Figure 6). The pre-anneal hysteresis loop (blue) clearly shows the bistable turn-on and turn-off, whereas the post-anneal hysteresis loop (red) lacks these sharp

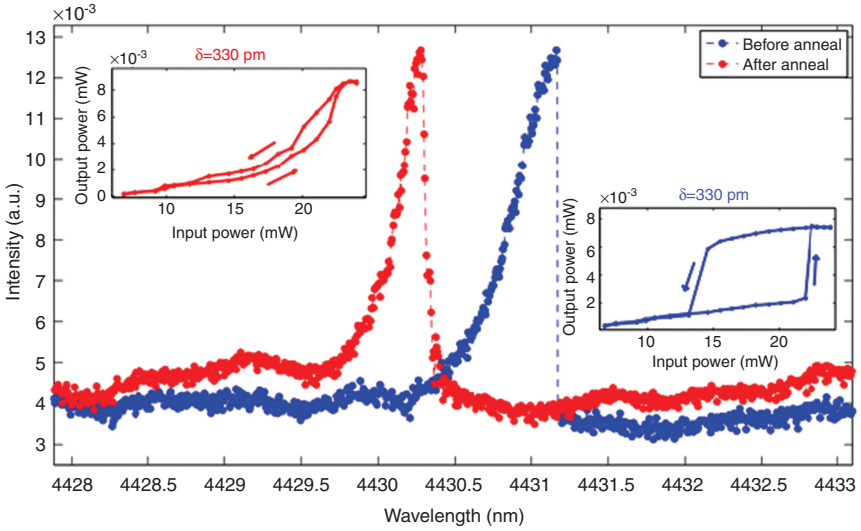


**Figure 6** Cavity spectrum taken before (blue) and after (red) annealing in a $N_2$ environment. The blue spectrum and corresponding hysteresis loop (taken at δ =330) show clear evidence of bistability, while the red spectrum and corresponding hysteresis loop (taken at the same detuning of δ =330 pm) indicate that bistability is no longer present. Taken from reference [11].

bistable transitions. Some hysteresis is present in the post-anneal, indicating that some small sources of absorption still remain in the cavity [30], but bistability is no longer seen after annealing treatment. We therefore concluded that water moisture and/or SiH bonds on the surface of the silicon device layer is the primary source of absorption that led to bistability.

Though main objective in performing these micro-electronic treatments on our cavities was to elucidate the source of the observed bistability, we also discovered a method to improve the quality factor of the photonic crystal cavities, from an initial Q of 11,500 to 29,300. In addition, after these treatments, we were able to measure a photonic crystal cavity with $s$=0.2$a$ with a theoretical Q=80,000 that had not been visible pre-treatment (likely due to the small absorption-limited Q before the treatment), again showing the utility of our treatments in minimizing losses. A Q-factor of 45,000 was measured in this case. We believe that micro-electronic treatments and annealing processes discussed here will be of great utility in mid-IR Si photonics, and may enable the realization of ultra-high Q cavities of interest for many mid-IR applications.

## 4 Grating-coupled ring resonators in a SOS platform

As mentioned previously, many mid-IR photonics applications may require an integrated, on-substrate platform that does not rely on membrane-type devices such as the ones discussed so far. For example, while disk and ring resonators can be realized in the SOI platform (Figure 7),


**Figure 7** A suspended wheel-type disk resonator fabricated in a silicon-on-insulator (SOI) platform for the mid-IR. Removal of the oxide layer is required for high performance, since oxide is lossy throughout much of the mid-IR.

the fabrication procedure for these devices is complicated by the need to remove the $SiO_2$ sacrificial layer. Silicon-on-sapphire (SOS) is an attractive platform for on-substrate mid-infrared photonics, due to the low loss of sapphire through much of the mid-IR [2, 4]. We recently demonstrated grating-coupled SOS microring resonators operating in the 4.3-4.6 µm range, with quality (Q) factors well above 100,000 [18]. We summarize some of these results below.

Grating couplers can provide highly efficient coupling of light from a free space beam into an optical waveguide. This method has already been well studied at telecom wavelengths [42, 43], with coupling losses as low as -0.75 dB experimentally attained by Luxtera [44]. Additionally, grating couplers can be placed anywhere on the chip, affording flexibility in input/output coupling location. Our grating couplers were designed to couple light from our QCL (CW emission from 4.3–4.6 µm) at normal incidence into a waveguide etched into the Si device layer of our SOS, with thickness $t$=812 nm. While higher in-coupling efficiencies can be achieved for an off-axis incidence, we chose normal incidence for ease of experimental characterization. The grating coupler design was optimized in Comsol using NOMAD [45], a global optimization algorithm. A linear taper function was applied both to the periodicity and the duty cycle of the grating structure, which consisted of fully etched slits in the Si device layer. The theoretical coupling efficiency of the optimized grating at normal incidence for a fully-etched geometry was 40%, with a bandwidth of about 150 nm (Figure 8, inset). The grating slits are 50 µm wide, so as to accommodate our relatively large beam (about 30 µm in diameter) and need to be oriented in the same direction as the polarization of our horizontally polarized input laser.

The devices were fabricated on a silicon-on-sapphire substrate with silicon device layer thickness of 812 nm (IQEP Silicon, Ltd.). ZEP (Zeon Corp.) was used as a mask for electron-beam lithography. A standard 125 kV electron-beam lithography tool (Elionix F-125) was used to define patterns in the ZEP layer. A single step etch process was performed in the STS ICP-RIE, and the resist was removed using Piranha etch. Then, we performed the Piranha/HF cycling procedure (three times), as mentioned in Section 3, in order to reduce surface roughness and surface absorption states. This procedure was found to have a significant impact on the performance for these devices [18].

An optical micrograph of one of our full devices (grating-coupled ring resonator) is shown in Figure 9. The two insets show SEM images of the grating coupler and the coupling region between the ring and bus waveguide. The grating coupler, taper region, ridge waveguide,

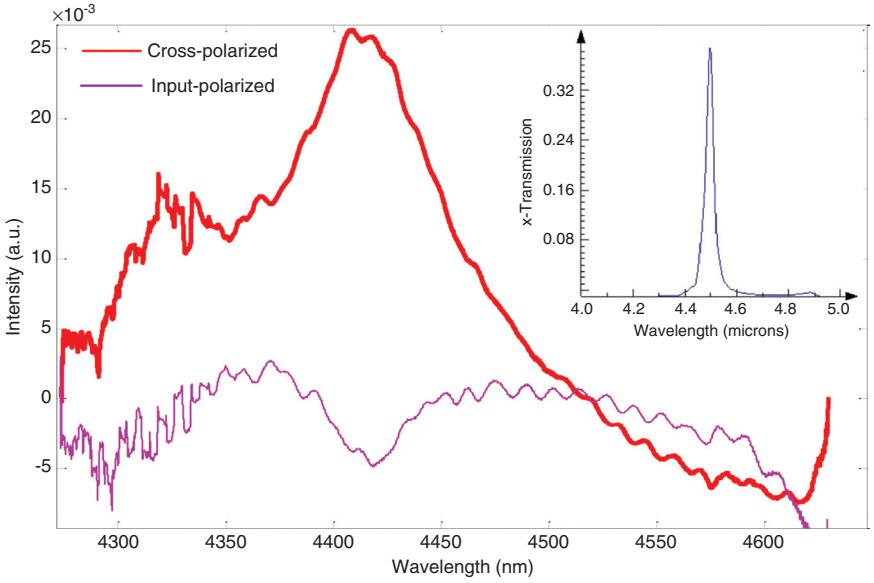


**Figure 8** Resonant scattering response of a grating coupler. A peak is seen in cross polarization, and a dip seen in input polarization, if the grating coupler couples light within the laser tuning range. Inset shows theoretical transmission response of grating coupler.

and ring resonator all are fully etched into the Si device layer with thickness $t$=812 nm. The coupling waveguide and ring resonator both have a width $w$=1.5 μm, and the ring radius $r$=60 μm. The grating slits are 50 μm wide, and the taper region between the grating and coupling waveguide is 500 μm long. Rings with gaps $d$ between the coupling waveguide and ring resonator varying between 300 and 700 nm were fabricated. Since the bandwidth of the grating is smaller than the mode-hop free tuning range of our laser, the grating geometry was varied from device to device in order to cover the laser's tuning range. A horn-shaped coupler consisting of a 750 μm long linear taper with a width of 50 μm at the output end was used to improve collection of light at the output.

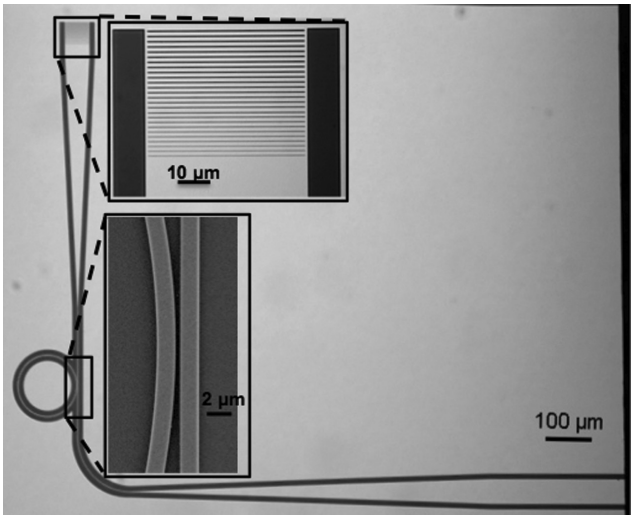


**Figure 9** Optical image of a representative device, consisting of a ring resonator coupled to a waveguide with a grating coupler (top inset) on input end and horn-coupler on the output end. Bottom inset shows coupling region between ring resonator and bus waveguide, with a gap of 400 nm in this case. Adapted from reference [18].

A grating coupler can be viewed as a one-dimensional photonic crystal cavity with very low quality factor. Therefore, its performance can also be characterized using cross-polarized resonant-scattering setup described earlier: the signal reflected from the coupler will appear as a resonant peak in the reflection spectrum of the coupler, Alternatively, if the setup is operated in parallel-polarized (not cross-polarized) configuration, with both polarizers aligned, the reflection spectrum will feature a dip, corresponding to the wavelength range where the coupling is maximized. Results from this characterization for a particular grating coupler are shown in Figure 8, with the background removed. As predicted, the operating range of the coupler corresponds to the peaks in cross polarization (CP) measurement and a dip in parallel-polarization (IP) measurement. Coupling efficiency was difficult to gauge from this experiment, but we roughly estimate coupling efficiencies on the order of 5–10%. The experimental efficiency is much lower than the theoretical one due to substantial differences between the fabricated dimensions of the grating coupler and those of the design.

After the optimization of grating coupler was accomplished, the complete devices were characterized as follows: light from a tunable continuous-wave quantum

cascade laser (QCL) from Daylight Solutions, Inc., with emission from 4.27 to 4.63 μm[1], is sent through a ZnSe objective (NA of 0.22) and focused onto the input grating. A second ZnSe lens (NA of 0.64) is placed at right angle to the first lens in order to collect light from the end facet with the horn-taper coupler. Finally, the light is focused onto a thermoelectrically cooled HgCdTe (MCT) detector. The horn-coupler was used in the out-coupling section to simplify the characterization procedure.

Transmission data from our resonators are shown in Figure 10 [18]. Results from a device with a value of $d$=300 nm is shown. The experimentally obtained transmission spectra were fitted to theoretical curves obtained by solving a set of coupled mode equations [46] that take into account the scattering-induced coupling of clock-wise and counter-clock-wise propagating modes, which can be observed as mode-splitting for very high-Q resonators. We measured total Q-factors as high as $Q_t$ =151,000, and intrinsic Q-factors as high as $Q_0$=278,000. These Q-values are, to our knowledge, the highest measured in the 4–5 μm wavelength range in Si. The performance of these devices was optimized by using the resist reflow technique (which minimizes surface roughness) during fabrication [47]. In our case, resist reflow consisted of a 5-min post-lithography bake in an oven at 140°C. Because of the fine features within our grating couplers, we had to use lower bake temperatures for reflow than those typically used for microresonators [47]. After the reflow, the sample underwent etching, cleaving, and the Piranha etch-HF acid cycling procedure described earlier, which we also found to have a significant impact on the Q-factors of these devices.

We demonstrated another variant on grating-coupled SOS ring resonators by partially etching rather than fully etching the Si. This resulted in devices that have a Si "pedestal" in cross section. Because of this, the optical mode is more strongly confined to the Si, though the waveguide was widened in order to accommodate the pedestal. The higher confinement in Si leads to lower loss since less of the mode interacts with the comparatively lossier sapphire substrate. We made grating-coupled SOS ring resonators with a 510 nm partial etch, and a waveguide width of 2.8 μm, and coupling gaps $d$ of 600 nm, 800 nm, and 1000 nm. Other than the grating parameters (period and slit widths), which needed to be changed to accommodate the partial etch, all other parameters were kept the same as in the fully etched case. All part of the device (grating, taper, waveguide, ring) were etched to the same depth. Results from one of our partially etched devices, with no post-fabrication treatments performed, are shown in Figure 11. No resist reflow was performed during the fabrication. Remarkably, the as-processed Q-factors on this sample were similar to devices made with resist reflow and Piranha-HF cycling, with $Q_t$ as high as 188,000 and $Q_0$ as high as 275,000. We attribute this to the fact that more of the mode is confined to the Si, thus reducing the overlap with the surface and the silicon-sapphire interface. Afterwards, Piranha-HF cycling was performed, but it had very little impact on the Q-factors of the device. Performing even shallower partial etches may have an even greater impact on Q.

Using our Q values, we can estimate the loss of our ring resonators to be about 0.74 dB/cm at 4.5 μm. We note

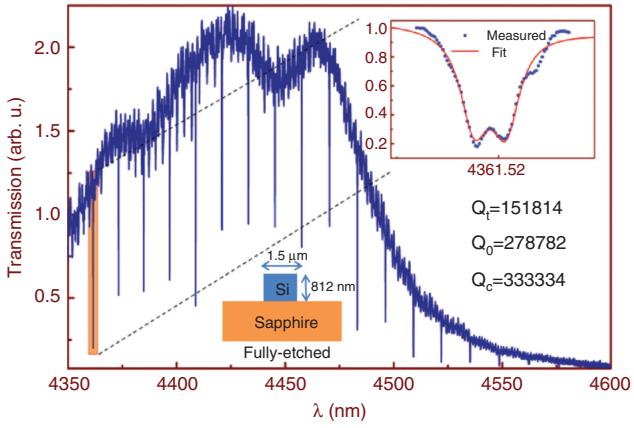


**Figure 10** Transmission measurement of fully-etched device with $d$=300 nm, fabricated using resist reflow and post-fabrication Piranha-HF cycling. The reflow results in higher Q-factors, with a maximum loaded $Q_t$ of 151,000 and intrinsic $Q_0$ of 278,000, as shown in the inset. Adapted from reference [18].

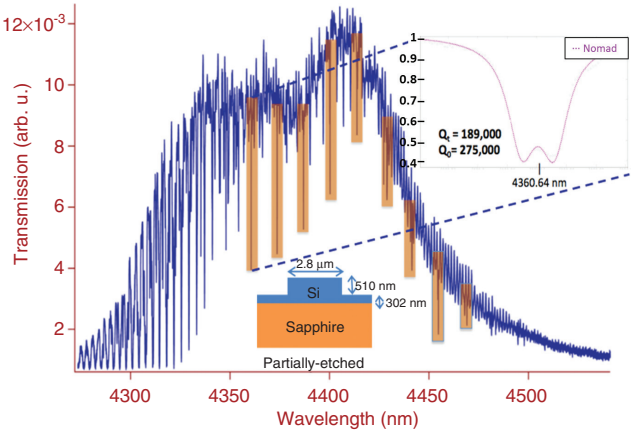


**Figure 11** Transmission measurement of partially etched device, with partial etch of depth 510 nm. No resist reflow or post-processing Piranha etch/HF dip cycling is performed for these devices. Intrinsic Q-factors of 188,000 and total Q-factors of 275,000 are achieved.

1 Our QCL was rebuilt in the time between this experiment and the photonic crystal cavity experiment, resulting in slightly different tuning ranges.

that this loss value takes into account not only light scattering (due to surface roughness) and material absorption (due mostly to surface states), but also bending losses of the ring resonator. The latter, however, are negligible in large diameter devices that we studied. This loss value is slightly higher than the lowest waveguide loss values reported for silicon devices at the mid-IR (0.6 dB/cm at 3.39 μm in the case of SOI waveguides [19]). Our comparatively higher losses may be due to scattering losses from twinning defects inherent in SOS [48]. Figure 12 shows a SEM image of the top surface and sidewalls of our device. Roughness on the sidewalls, as well as graininess on the top surface (likely due to twinning defects), can be seen. Using thicker Si device layers can minimize the effect of the twinning defects, since these defects originate at the silicon-sapphire interface [48]. Additionally, further optimization of the fabrication process needs to be done in order to reduce sidewall roughness and thereby increase resonator Q-factors even further.

## 5 Summary and outlook

We have presented our recent work on the development of Si photonic devices in operational at the mid-IR, focused on the 4–5 μm range. Devices in two different platforms – photonic crystal cavities in a Si membrane platform and grating-coupled ring resonators in a SOS platform – are discussed. We have also focused on the experimental techniques we use to characterize and test our devices, including scanning resonant scanning microscopy and grating-coupled transmission measurements. The next step is to transfer devices such as these to on-chip applications, e.g. on-chip spectrometers for trace gas sensing or high-power photonic chips for data communications. An on-chip spectrometer operational at 3.8 μm using mid-infrared Si waveguides and arrayed-waveguide gratings was demonstrated recently by M. Muneeb and colleagues at Ghent University, IMEC, and the University of Southhampton [49]. Using high-Q factor resonators for an on-chip spectrometer, such as in [50] would greatly decrease the footprint of the spectrometer.

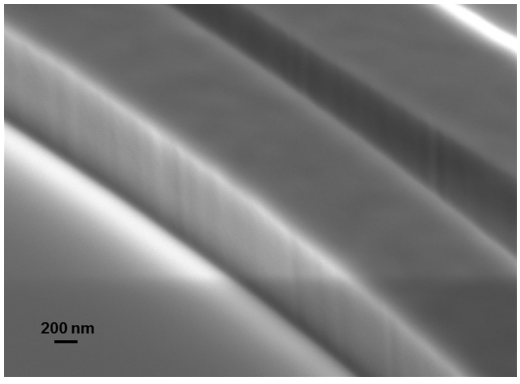


**Figure 12** Scanning electron micrograph of sidewalls and top surface of a fully etched device. Graininess on the top surface, due to twinning defects in the SOS [48], can be seen, along with roughness on the sidewalls.

For truly integrated mid-infrared devices, active devices such as lasers, detectors, and modulators have to be integrated on-chip. In the case of on-chip modulators, it is possible to use Si itself for the modulator, as demonstrated by M. van Camp and colleagues at IBM Watson Labs, who demonstrated an electrorefractive Si modulator at 2.165 μm, with modulation speeds of up to 3 GHz [51]. Note that modulators at wavelengths above 3 μm will likely require an electro-absorptive configuration [51, 52]. However, for the case of sources and detectors, hybrid integration will be required, since mid-IR sources and detectors are largely composed of III-V materials. Recently, researchers at Ghent University and Universite Montpellier demonstrated the integration of GaInAsSb photodiodes and photodetectors operating around 2.2 μm to a SOI platform using BCB adhesive bonding [53]. However, much more work needs to be done in integrating QCLs and longer-wavelength detectors to Si-based chips. Lastly, the use of graphene, due to graphene's broad absorption spectral bandwidth and ultrafast response time, is a promising avenue for on-chip silicon-based modulators [54] and detectors [55] at the mid-IR.

Another direction that is also being explored is nonlinear frequency conversion in mid-IR photonic devices. The mid-infrared wavelength regime is an ideal wavelength range to achieve nonlinear frequency conversion in Si, due to the lack of two-photon absorption at wavelengths above the two-photon band-edge of 2.2 μm. In the last few years, multiple research groups have demonstrated parametric amplification and parametric generation around 2.2 μm in Si waveguides. For example, in 2010, Xiaoping Liu and colleagues at IBM Watson Labs and Columbia University demonstrated parametric amplification in 4 mm-long Si waveguides [8]. A broadband parametric gain of 25.4 dB was achieved, which was large enough to overcome insertion losses, resulting in an overall net off-chip gain of 13 dB. Similarly, in 2010, Sanja Zlatanovic and colleagues at UCSD and UCF demonstrated four-wave mixing in 3.8 mm-long Si waveguides [6]. More recently, Xiaoping Liu and colleagues at IBM Research Labs, Columbia University, and Ghent University demonstrated down-conversion of mid-infrared photons at 2.44 μm to telecom photons at 1.62 μm through four-wave mixing in silicon

waveguides [56], with a parametric gain of 19 dB. This type of parametric down-conversion to the telecom regime can be highly advantageous for compact mid-IR devices, as telecom detectors are more sensitive and more energy-efficient (since cryogenic cooling is not required) than their mid-IR counterparts.

Perhaps the most exciting application of mid-IR photonics is the realization of integrated frequency combs operating in mid-IR range. By using high Q-factor mid-infrared Si resonators such as the ones described earlier in this review, nonlinear frequency conversion can be made much more efficient, allowing for optical parametric oscillation to occur with relatively low power thresholds (tens of mW inside the device). The generation of many-sideband optical parametric oscillators in high-Q factor microresonators has already been demonstrated in several different material systems at the telecom wavelength range, including Hydex glass microrings [57], SiN microrings [58], and silica microtoroids [59]. Recently, C. Wang and colleagues have demonstrated the first mid-infrared frequency comb, based on a $MgF_2$ crystalline microresonator, operational around 2.5 μm [60]. We anticipate that Si-based optical parametric oscillators operational at the wavelengths produced by commercial QCLs (>3.5 μm) will be demonstrated in the near future. This development would be especially useful for on-chip trace gas sensing, as a mid-infrared frequency comb could act as both a multichannel generator and spectral analysis tool [61].

**Acknowledgments:** We would like to thank the other authors of the papers discussed here, Irfan Bulu and Rick Leijssen. We would also like to thank Qimin Quan, Leonard Kogos, Parag Deotare, Ian Burgess, Julie Frish, and Mickey Frish for helpful discussions and assistance with fabrication. Devices were fabricated at the Center for Nanoscale Systems at Harvard University. This work is supported in part by the NSF CAREER grant (ECCS-0846684), SBIR Contract W911SR-11-C-0008 from the U. S. Army, and generous support from Schlumberger-Doll Research Center (Cambridge, MA).

Received June 26, 2013; accepted November 3, 2013; previously published online November 28, 2013

## References

[1] Tsay C, Mujagić E, Madsen CK, Gmachl C, Arnold C. Mid-infrared characterization of solution-processed $As_2S_3$ chalcogenide glass waveguides. Opt Exp 2010;18:15523–30.
[2] Soref R, Emelett S, Buchwald W. Silicon waveguided components for the long-wave infrared region. J Opt A: Pure and Appl Opt 2006;8:840–8.
[3] Palik ED. Handbook of Optical Constants of Solids, Volume 1. San Diego, CA: Academic Press, 1985.
[4] Soref R. Mid-infrared photonics in silicon and germanium. Nat Photonics 2010;4:495–7.
[5] Jalali B. Silicon photonics: Nonlinear optics in the mid-infrared. Nat Photonics 2010;4:506–8.
[6] Zlatanovic S, Park JS, Moro S, Chavez Boggio JM, Divliansky IB, Alic N, Mookherjea S, Radic S. Mid-infrared wavelength conversion in silicon waveguides using ultracompact telecom-band-derived pump source. Nat Photonics 2010;4:561–4.
[7] Raghunathan V, Borlaug D, Rice R, Jalali B.. Demonstration of a mid-infrared silicon Raman amplifier. Opt Exp 2007;15:14355–62.
[8] Liu X, Osgood RM, Vlasov YA, Green, WM. Mid-infrared wavelength conversion in silicon waveguides using ultracompact telecom-band-derived pump source. Nat Photonics 2010;4:557–60.
[9] Hon NK, Soref R, Jalali B. The third-order nonlinear optical coefficients of Si, Ge, and $Si_{1-x}Ge_x$ in the midwave and longwave infrared. J Appl Phys 2011;110:011301.
[10] Shankar R, Leijssen R, Bulu I, Lončar M. Mid-infrared photonic crystal cavities in silicon. Opt Exp 2011;19:5579–86.
[11] Shankar R, Bulu I, Leijssen R, Lončar M. Study of thermally-induced optical bistability and the role of surface treatments in Si-based mid-infrared photonic crystal cavities. Opt Exp 2011;19:24828–37.
[12] Reimer C, Nedeljkovic M, Stothard DJM, Esnault MO, Reardon C, O'Faolain L, Dunn M, Mashanovic GZ, Krauss TF. Mid-infrared photonic crystal waveguides in silicon. Opt Exp 2012;20:29361–8.
[13] Baehr-Jones T, Spott A, Ilic R, Spott A, Penkov B, Asher W, Hochberg M. Silicon-on-sapphire integrated waveguides for the mid-infrared. Opt Exp 2010;18:12127–35.
[14] Spott A, Liu Y, Baehr-Jones T, Ilic R, Hochberg M. Silicon waveguides and ring resonators at 5.5 mu m. Appl Phys Lett 2010;97:213501.
[15] Cheng Z, Chen X, Wong CY, Xu K, Fung CKY, Chen YM, Tsang HK. Mid-infrared grating couplers for silicon-on-sapphire waveguides. IEEE Photon J 2012;4:104–13.
[16] Li F, Jackson SD, Grillet C, Magi D, Hudson D, Madden SJ, Moghe Y, O'Brien C, Read A, Duvall SG, Atanackovic P, Eggleton BJ and Moss DJ. Low propagation loss silicon-on-sapphire waveguides for the mid-infrared. Opt Exp 2011;19:15212–20.
[17] Wong CY, Cheng Z, Chen X, Xu F, Fung CKY, Chen YM, Tsang HK. Characterization of mid-infrared silicon-on-sapphire microring resonators with thermal tuning. IEEE Photon J 2012;4:1095–102.
[18] Shankar R, Bulu I, Lončar M. Integrated high-quality factor silicon-on-sapphire ring resonators for the mid-infrared. Appl Phys Lett 2013;102:051108.
[19] Mashanovic GZ, Milosevic MM, Nedeljkovic M, Owens N, Xiong B, Teo EJ, Hu Y. Low loss silicon waveguides for the mid-infrared. Opt Exp 2011;19:7112–9.

[20] Khan S, Chiles J, Ma J, Fathpour S. Silicon-on-nitride waveguides for mid- and near-infrared integrated photonics. Appl Phys Lett 2013;102:121104.
[21] Lin P, Singh V, Kimerling L, Agarwal A. Planar silicon nitride mid-infrared devices. Appl Phys Lett 2013;102:251121.
[22] Chang YC, Paeder V, Hvozdara L, Hartmann JM, Herzig HP. Low-loss germanium strip waveguides on silicon for the mid-infrared. Opt Lett 2013;37:2883–5.
[23] Lin P, Singh V, Cai Y., Kimerling L, Agarwal A. Air-clad silicon pedestal structures for broadband mid-infrared microphotonics. Opt Lett 2013;38:1031–3.
[24] Zhu X, Peyghambarian N. High-power ZBLAN glass fiber lasers: Review and prospect. Adv Opt Electron 2010;2010:23. Article ID 501956. DOI:10.1155/2010/501956.
[25] Akahane Y, Asano T, Song BS, and Noda S. High-q photonic nanocavity in a two-dimensional photonic crystal. Nat Photon 2003;425:944–77.
[26] McCutcheon M, Rieger GW, Cheung IW, Young JF, Dalacu D, Frederick S, Poole PJ, Aers GC, Williams RL. Resonant scattering and second-harmonic spectroscopy of planar photonic crystal microcavities. Appl Phys Lett 2005;87:22110.
[27] Deotare PB, McCutcheon MW, Frank IW, Khan M, Loncar M. High quality factor photonic crystal nanobeam cavities. Appl Phys Lett 2009;94:121106.
[28] Galli M, Portalupi SL, Belotti M, Andreani LC, O'Faolain L, Krauss TF. Light scattering and Fano resonances in high-Q photonic crystal nanocavities. Appl Phys Lett 2009;94:071101.
[29] Babinec TM, Hausmann BJM, Khan M, Zhang Y, Maze JR, Hemmer PR, Loncar M. A diamond nanowire single-photon source. Nat Nano 2010;5:195–9.
[30] Notomi M, Shinya A, Mitsugi S. Kira G, Kuramochi E, Tanabe T. Optical bistable switching action of Si high-Q photonic-crystal nanocavities. Opt Exp 2005;13:2678–87.
[31] Haret LD, Tanabe T, Kuramochi E, Notomi M. Extremely low power optical bistability in silicon demonstrated using 1D photonic crystal nanocavity. Opt Exp 2009;17:21108–17.
[32] Uesugi T, Song BS, Asano T, Noda S. Investigation of optical nonlinearities in an ultra-high-Q Si nanocavity in a two-dimensional photonic crystal slab. Opt Exp 2006;14:377–86.
[33] Barclay PE, Srinivasan K, Painter O. Nonlinear response of silicon photonic crystal microresonators excited via an integrated waveguide and fiber taper. Opt Exp 2005;13:801–20.
[34] Almeida VR, Lipson M. Optical bistability on a silicon chip. Opt Lett 2004;29:2387–9.
[35] Weidner E, Combrie S, de Rossi A, Tran NVQ, Cassette S. Nonlinear and bistable behavior of an ultrahigh-Q GaAs photonic crystal nanocavity. Appl Phys Lett 2007;90:101118.
[36] Pernice WHP, Li M, Tang HX. Time-domain measurement of optical transport in silicon micro-ring resonators. Opt Exp 2010;18:18438–52.
[37] Schroeder DK, Semiconductor material and device characterization. Hoboken, NJ, USA: Wiley Interscience, 2006.
[38] de Rossi A, Lauritano M, Combrie S, Tran QV, Husko C. Interplay of plasma-induced and fast thermal nonlinearities in a GaAs-based photonic crystal nanocavity. Phys Rev A 2009;79:043818.
[39] Borselli M, Johnson TJ, Painter O. Measuring the role of surface chemistry in silicon microphotonics. Appl Phys Lett 2006;88:131114.
[40] Yamashita Y, Namba K, Nakato Y, Nishioka Y, Kobayashi H. Spectroscopic observation of interface states of ultrathin silicon oxide. J Appl Phys 1996;79:7051–57.
[41] Froitzheim H, Lammering H, Gunter HL. Energy-loss-spectroscopy studies on the adsorption of hydrogen on cleaved Si(111)-(2×1) surfaces. Phys Rev B 1983;27:2278–84.
[42] McNab S, Moll N, Vlasov Y. Ultra-low loss photonic integrated circuit with membrane-type photonic crystal waveguides. Opt Exp 2003;11:2927–39.
[43] Vermeulen D, Selvaraja S, Verheyen P, Lepage G, Bogaerts W, Absil P, Van Thourhout D, Roelkens G. High-efficiency fiber-to-chip grating couplers realized using an advanced CMOS-compatible Silicon-On-Insulator platform. Opt Exp 2010;18:18278–83.
[44] Mekis A, Abdalla S, Foltz D, Gloeckner S, Hovey S, Jackson S, Liang Y, Mack M, Masini G, Peterson M, Pinguet T, Sahni S, Sharp M, Sun P, Tan D, Verslegers L, Welch BP, Yokoyama K, Yu S, De Dobbelaere, PM. A CMOS photonics platform for high-speed optical interconnects. IEEE Photonics Conference (IPC), 2012;23–27.
[45] Le Digabel S. Algorithm 909: Nomad: Nonlinear optimization with the mads algorithm. ACM Trans Math Softw 2011; 44:1–44.
[46] Kippenberg, TJ, Spillane SM, Vahala KJ. Modal coupling in traveling-wave resonators. Opt Lett 2002;27:1669–71.
[47] Borselli M, Johnson T, Painter O. Beyond the Rayleigh scattering limit in high-q silicon microdisks: theory and experiment. Opt Exp 2005;13:1515–30.
[48] Imthurn G. "The History of Silicon-on-Sapphire," white paper for Peregrine Semiconductor Corporation, 2007.
[49] Muneeb M, Chen X, Verheyen P, Lepage G, Pathak S, Ryckeboer E, Malik A, Kuyken B, Nedeljkovic M, Van Campenhout J, Mashanovich GZ, Roelkens G. Demonstration of silicon-on-insulator mid-infrared spectrometers operating at 3.8 um. Opt Exp 2013;21:11659–69.
[50] Deotare PB, Kogos LC, Bulu I, Loncar M. Photonic crystal nanobeam cavities for tunable filter and router applications. IEEE J Sel Topics in Quant Electron 2013;19:3600120.
[51] Van Camp MA, Assefa S, Gill DM, Barwicz T, Shank SM, Rice PM, Topuria T, Green WM. Demonstration of electrooptic modulation at 2165 nm using a silicon Mach-Zender interferometer. Opt Exp 2012;20:28009–16.
[52] Nedeljkovic M, Soref R, Mashanovich GZ. Free-carrier electro-refraction and electro-absorption modulation predictions for silicon over the 1–14 μm infrared wavelength range. IEEE Photon J 2011;3:1171–80.
[53] Gassenq A, Hattasan N, Cerutti L, Rodriguez JB, Tournie E, Roelkens E, Study of evanescently coupled and grating assisted GaInAsSb photodiodes integrated on a silicon photonic chip. Opt Exp 2012;20:11665–72.
[54 Liu M, Yin X, Ulin-Avila E, Geng B, Zentgraf T, Ju L, Wang F, Zhang X. A graphene-based optical modulator. Nature 2011;474:64–7.
[55] Gan X, Shiue RJ, Gao Y, Meric I, Heinz T, Shepard K, Hone J, Assefa S, Englund D. Chip-integrated ultrafast graphene photodetector with high responsivity. Nat Photon 2013;7: 883–87.
[56] Liu X, Kuyken B, Roelkens G, Baets R, Osgood RM, Green WM. Bridging the mid-infrared-to-telecom gap with silicon nanophotonic spectral translation. Nat Photon 2012;6:667–7.

[57] Razzari L, Duchesne D, Ferrera M, Morandotti R, Chu S, Little BE, Moss DJ. Cmos-compatible integrated optical hyper-parametric oscillator. Nat Photon 2009;4:41–5.
[58] Levy JS, Gondarenko A, Foster MA, Turner-Foster AC, Gaeta AL, Lipson M. Cmos-compatible multiple-wavelength oscillator for on-chip optical interconnects. Nat Photon 2009;4:37–40.
[59] Del'Haye P, Herr T, Gavartin E, Gorodetsky ML, Holzwarth R, Kippenberg TJ. Octave spanning tunable frequency comb from a microresonator. Phys Rev Lett 2011;107: 063901.
[60] Wang CY, Herr T, Del'Haye P, Schliesser A, Hofer J, Holzwarth R, Hänsch, TW, Picquè N, Kippenberg TJ. Mid-infrared optical frequency combs at 2.5 um based on crystalline microresonators. Nat Commun 2013;4:1345.
[61] Kippenberg TJ, Holzwarth R, Diddams SA. Microresonator-based optical frequency combs. Science 2011;332:555–9.